Comparison of Direct Covariance Flux Measurements from an Offshore Tower and a Buoy

MARTIN FLÜGGE,* MOSTAFA BAKHODAY PASKYABI, AND JOACHIM REUDER

University of Bergen, and Bjerknes Centre for Climate Research, Bergen, Norway

JAMES B. EDSON

University of Connecticut, Groton, Connecticut

ALBERT J. PLUEDDEMANN

Woods Hole Oceanographic Institution, Woods Hole, Massachusetts

ABSTRACT

Direct covariance flux (DCF) measurements taken from floating platforms are contaminated by wave-induced platform motions that need to be removed before computation of the turbulent fluxes. Several correction algorithms have been developed and successfully applied in earlier studies from research vessels and, most recently, by the use of moored buoys. The validation of those correction algorithms has so far been limited to short-duration comparisons against other floating platforms. Although these comparisons show in general a good agreement, there is still a lack of a rigorous validation of the method, required to understand the strengths and weaknesses of the existing motion-correction algorithms. This paper attempts to provide such a validation by a comparison of flux estimates from two DCF systems, one mounted on a moored buoy and one on the Air–Sea Interaction Tower (ASIT) at the Martha's Vineyard Coastal Observatory, Massachusetts. The ASIT was specifically designed to minimize flow distortion over a wide range of wind directions from the open ocean for flux measurements. The flow measurements from the buoy system are corrected for wave-induced platform motions before computation of the turbulent heat and momentum fluxes. Flux estimates and cospectra of the corrected buoy data are found to be in very good agreement with those obtained from the ASIT. The comparison is also used to optimize the filter constants used in the motion-correction algorithm. The quantitative agreement between the buoy data and the ASIT demonstrates that the DCF method is applicable for turbulence measurements from small moving platforms, such as buoys.

1. Introduction

Direct covariance flux (DCF) measurements are widely performed over land from fixed towers and other platforms (Stull 1988). Although different methods can be used for the estimation of turbulent fluxes—for example, the bulk aerodynamic method (e.g., Liu et al. 1979), the gradient method (e.g., Edson et al. 2004), and the inertial dissipation method (e.g., Yelland and Taylor 1996)—the DCF method provides the only direct approach (e.g., Crawford et al. 1993). In the coastal ocean, DCF measurements are usually taken from land-based towers close to the sea or from offshore towers in shallow water, such as the Swedish Östergarnsholm tower (Smedman et al. 1999; Högström et al. 2008); the U.S. Air Sea Interaction Tower (ASIT) off Martha's Vineyard, Massachusetts (Austin et al. 2002; Edson et al. 2007); and the German Forschungsplattformen in

Nord- und Ostsee (FINO) platforms (Neumann et al. 2003; Fischer 2006). A substantial advantage of these fixed platforms is that the DCF method can be applied without any motion correction. Most towers also supply continuous power and data communication and can provide real-time data over extended observation periods. They are, however, subject to flow distortion and turbulence injection by the support structure for certain wind directions.

Applying the DCF approach to measurements in the marine atmospheric boundary layer (MABL) farther offshore and in deeper waters requires the use of moored buoys or mobile platforms, such as ships or drifting buoys. Except for the mobile stable Research Platform (R/P) *FLIP* (*Floating Instrument Platform*; e.g., Miller et al. 2008), DCF measurements in the MABL over deep water have mostly been taken from ships (Mitsuta and Fujitani 1974; Fujitani 1981, 1985; Tsukamoto et al. 1990; Song et al. 1996; Fairall et al. 1997; Edson et al. 1998; Takahashi et al. 2005). These measurements are considerably affected by aerodynamic flow distortion induced by the vessel's superstructure (e.g., Yelland et al. 1998, 2002). The accuracy of corresponding flux estimates depends strongly on the geometry and dimension of the ship, the location of the flux sensors and their heights above sea level, and the angle between the incoming flow and the ship's bow (e.g., Yelland et al. 2002). To minimize these effects, the flux sensors are usually mounted on the foremast and data are only considered valid when the bow is pointed into the wind.

Even with optimal exposure of the sensors, the measurements from ships and other moving platforms are contaminated by the angular and translational velocities of the platform caused by wave-induced motion. This contamination must be removed before computation of the fluxes. The motion-correction procedure involves the application of an inertial measurement unit (IMU) that contains high-precision acceleration and angular rate sensors. The processed signals of these sensors are used to determine the platform's attitude angles and translational velocities. Those are added to the platform velocities in an Earth- or water-relative frame using data from a GPS or current meter, respectively (Edson et al. 1998). Because of high costs for the required IMU, the DCF method was not widely used for air–sea investigations until the middle of the 1990s, when less expensive IMUs became available.

To overcome the aforementioned limitations of ship-based flux measurements over a broad range of sea-state and weather conditions, researchers started to investigate the possibility of DCF measurements from buoys (Fujitani 1981; Dugan et al. 1991; Anctil et al. 1994). The first successful DCF measurements from a buoy with a gyro-controlled mast were performed during the Atlantic Tradewinds Experiment in 1969 (Dunckel et al. 1974).

Using a correction algorithm similar to Fujitani (1981), Dugan et al. (1991) and Anctil et al. (1994) proposed a setup for DCF measurements from buoys with a gimbaled motion sensor. Today, the DCF systems deployed on buoys are equipped with small, generally low-power-consuming motion packages that can easily be attached to the frame in a "strap down" mode of operation.

Despite obvious operational limitations, in particular with respect to power supply and the vulnerability of flux sensors while operating in a demanding marine environment close to the sea surface (e.g., salt deposition and corrosion), buoys equipped with DCF systems provide a number of advantages as measurement platforms. They can work autonomously for several months up to a year, and they can have a distinctly reduced flow distortion compared to offshore towers and ships (Weller et al. 2012; Bigorre et al. 2013). The deployment time can be extended by operating in duty cycles, where the devices are collecting data only for limited time periods (e.g., 20 min out of every hour), while staying in power-saving mode the rest of the time. Modern DCF systems are also supplied with GPS and wireless telemetry, thus enabling the researcher to follow the platform position and to receive real-time data onshore. Two-way communication is also being tested to allow event-driven periods of continuous operation. The Woods Hole Oceanographic Institution (WHOI) has developed surface buoys (Weller et al. 2012) with a long and successful history of long-term field deployments at remote ocean sites. These buoys are traditionally equipped with both meteorological and oceanographic sensors (e.g., Hosom et al. 1995; Colbo and Weller 2009) that provide time series of mean values that can be used to compute estimates of the surface fluxes using the bulk methods (e.g., Fairall et al. 1996). More recently, the buoys also have been instrumented with DCF systems for the assessment of the turbulent heat and momentum exchange at the air–sea interface during the Climate Variability and Predictability (CLIVAR) Mode Water Dynamic Experiment (CLIMODE; Marshall et al. 2009; Bigorre et al. 2013) and the Salinity Processes in the Upper Ocean Regional Study (SPURS; Farrar et al. 2015).

The gathered DCF data are usually corrected by well-established motion-correction algorithms (e.g., Edson et al. 1998; Miller et al. 2008) before calculating the variances and covariances. However, the algorithms have not yet been rigorously tested and validated against datasets from a fixed structure, mainly because the buoys are typically deployed in regions where such structures are not available. In general, all motion-correction algorithms require a careful empirical-based selection of relevant parameters. For example, the quality and performance of the complementary filtering
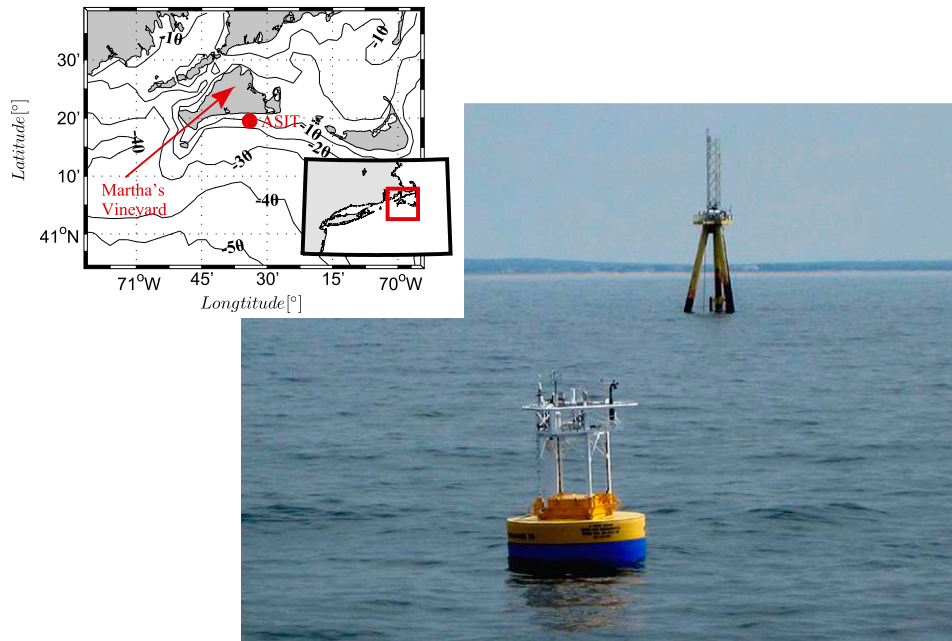
FIG. 1. The surface mooring deployed approximately 500 m in front of the ASIT at the MVCO. Meteorological sensors were mounted on a tower frame approximately 3.5 m above the sea surface. (upper left) A site map of Martha's Vineyard and the ASIT. The tower is located 3.2 km off the island's south shore in a water depth of 15 m.

method (Edson et al. 1998) used in this study depends strongly on the proper choice of the filter cutoff frequency, which is a function of both the platform's dynamics and the environmental forcing. Usually, the cutoff frequency is chosen based upon a similar research setup carried out in earlier studies, or by an empirical analysis of the IMU's rate sensor and accelerometer output (e.g., Schulz et al. 2005; Miller et al. 2008).

This paper presents a comparison of DCF measurements performed from a surface buoy and the Air–Sea Interaction Tower at the Martha's Vineyard Coastal Observatory (MVCO). Measurements from the surface buoy are corrected by the motion-correction algorithm of Edson et al. (1998) and compared to DCF measurements from a similar system that was mounted on the nearby ASIT. As the ASIT is a rigid platform, the tower measurements provided a reference dataset without contamination of wave-induced platform motions. Using both datasets, this study presents the best choice of the correction algorithm's cutoff frequency for a DCF system mounted on a specific moored buoy. It is also shown that the direction of the dominant waves can be estimated with a high degree of confidence from the mooring's IMU (a MotionPak II by Systron Donner) output alone. The experimental setup is described in section 2, and an overview of the data processing is given in section 3. Section 4 presents the flux comparisons

between the surface buoy and the ASIT. A discussion of the flux comparisons is given in section 5.

2. Experiment

a. Site and deployment

The campaign took place between 12 April and 29 June 2010 in the vicinity of the MVCO as shown in Fig. 1. The MVCO ASIT is located 3.2 km off Martha's Vineyard's south coast in a water depth of 15 m. The ASIT is specifically designed as a low-profile structure so that flow distortions induced by the tower structure itself are minimized with respect to the dominant direction of the incoming wind (Edson et al. 2007). The tower was equipped with a DCF system on a downward-facing boom, and flux measurements were obtained 3.75 m above the mean sea surface. During a tidal cycle, the change in sea surface elevation is approximately ±0.5 m at the measurement site. Having continuous power supply at the ASIT, DCF measurements were recorded at 20 Hz for three successive 20-min periods per hour.

To investigate the quality of the DCF measurements from small floating platforms, a surface buoy was moored approximately 500 m southwest of the ASIT (Fig. 1). The buoy and the configuration of the meteorological sensors were similar to the CLIMODE field study where the buoy was deployed in, and periodically

just north of, the meandering Gulf Stream for over one year (see Marshall et al. 2009; Weller et al. 2012; Bigorre et al. 2013; Edson et al. 2013). The buoy has a diameter of 2.7 m and is made of Surlyn closed-cell foam. A well in the center of the buoy accommodates the dataloggers and batteries for the instruments. Both Air–Sea Interaction Meteorology (ASIMET; Hosom et al. 1995; Colbo and Weller 2009) and DCF sensors were mounted on an open tower frame approximately 3.5 m above the sea surface. The ASIMET sensors included an R. M. Young propeller anemometer, mounted on the front, portside corner of the tower, and a Gill 2D sonic (WindObserver) mounted at the center front. The DCF system consisted of a Gill R3-50 sonic anemometer mounted on the starboard side of the tower and an open path gas analyzer (LI-COR 7500), placed next to the sonic anemometer.

A wind vane attached to the buoy kept the sensors faced into the mean wind direction. For the type of buoy used in the present study, the asymmetry of the central well creates a torque that slightly counteracts the effect of the wind vane (Bigorre et al. 2013). As a result, the buoy tends to orient itself with an offset angle of 15°–30° to the right of the incoming wind. The DCF system measures the three-dimensional wind vector relative to the right-handed coordinate frame of the instrument (i.e., x axis pointing forward along the major axis of the instrument, y axis pointing to the port side, and z axis pointing upward). The DCF system was operated at 20 Hz and averaged to 5 Hz before storage, and the runs were acquired in a duty cycle of 20 min at the beginning of every hour.

An IMU (MotionPak II) was housed in a watertight cylinder and attached to the base of the sonic anemometer, which placed it approximately 0.8 m below the sonic sampling volume. The IMU system measured the platform's attitude angles, angular velocity, and translational velocity due to water motion in a right-handed coordinate frame in which roll ϕ (rotation about x axis) is positive when the instrument port side is tilted up, pitch θ (rotation about y axis) is positive when the bow is tilted down, and yaw ψ (rotation about z axis) is positive counterclockwise. Note that ψ is defined positive for a right-handed rotation around the z axis, so a minus sign is applied to the compass reading.

b. Environmental conditions

The distribution of wind speeds and wind directions during the measurement period is shown in Fig. 2. The prevailing wind direction at the MVCO during the field deployment was southwest with wind speeds up to 13 m s^{-1}. Approximately 80% of the observed wind speeds fall within the 2–8 m s^{-1} range. Time series of wind speed and direction, and air pressure from the ASIT are shown in Figs. 3a–c. Wind directions for light
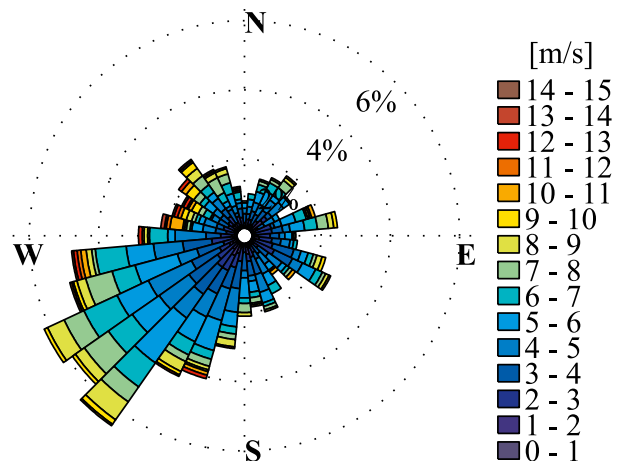

FIG. 2. Distribution of wind speed and wind direction recorded by the ASIT sonic anemometer. Data shown for averages over each 20-min run for the entire measurement period between 12 Apr and 29 Jun 2010.

winds below 2 m s^{-1} were highly variable, while winds in the range between 2 and 8 m s^{-1} were predominantly southwesterly. Wind speeds above 10 m s^{-1} are associated with the passage of low pressure systems with westerly to northwesterly winds.

In the course of the campaign, the air temperature recorded by the sonic anemometer was rising from approximately 10° to 25°C (Fig. 3d). Typical for spring and early summer, the marine atmospheric boundary layer at the deployment site was primarily neutral or slightly stable as a result of warming coastal waters and the advection of warmer air over the colder ocean (Crofoot 2004; Edson et al. 2007). Figure 3e shows that the heat flux between the ocean and the MABL was weak during the field campaign. Unstable conditions with upward-directed (positive) heat fluxes are associated with the passage of strong cold fronts, when cold air moves over the warmer ocean water.

The significant wave height (Fig. 3f) during the campaign was approximately 0.5 m when the wind speed was below 5 m s^{-1}, and 1.5 m for wind speeds between 5 and 10 m s^{-1}. For higher wind speeds, associated with the passage of low pressure systems, the significant wave height reached values between 2 and 3 m. Although the mooring did not experience wind speeds above 13 m s^{-1}, it was exposed to a variety of wave ages, ranging from young, wind-dominated developing seas to old, decaying seas, that is, swell.

3. Data processing

a. Data availability

For the comparison between the ASIT and the buoy measurements, only the first 20-min period starting at

every full hour has been included in our analysis of the tower data to match the dataset of the buoy operating in a corresponding duty cycle. Wind directions from 165° to 345° minimize the impact of flow distortion on the ASIT measurements as the sonic anemometer is upwind of the tower for these wind directions. Therefore, the comparative analysis of the datasets includes only data runs with wind approaching from this sector. Note that this does not limit the analysis to open ocean conditions as specified in Edson et al. (2007) as flow from west and northwest is affected by land. Both measurement systems will sense the same conditions; however, this is not an issue in the presented study. Moreover, runs with data gaps, faulty compass readings, and IMU sensor overrange in the buoy data were discarded from the collected datasets. The removal of data through quality control procedures left 1153 ASIT runs and 938 buoy runs available for the presented analysis, which is referred to as the reference dataset.

In an additional step, poor flux estimates were identified and removed from the reference dataset by analyzing the corresponding cospectra. For this purpose, the ogives (e.g., Oncley et al. 1996) of the momentum and heat fluxes were computed for each of the 20-min ASIT and motion-corrected buoy data runs. Briefly, the ogives were calculated as the cumulative integral of the cospectral estimates of the momentum and heat flux, from high to low frequencies before normalization by the magnitude of the corresponding covariances—that is, $\overline{u'w'}$ and $\overline{w'\theta'}$, respectively. The computed ogives are expected to level out and asymptotically approach the normalized value of 1 at low frequencies. For both datasets, we empirically chose a rejection criterion so that accepted ogives fall within a ±0.2 acceptance interval of this value, that is, $\int C_{u'w'}(f)\,df/\overline{u'w'} = 1 \pm 0.2$ and $\int C_{w'\theta'}(f)\,df/\overline{w'\theta'} = 1 \pm 0.2$, at the low-frequency end between $f = 2 \times 10^{-3}$ Hz (≈ 8 min) and $f = 0.87 \times 10^{-3}$ Hz (≈ 19 min). Values outside the acceptance interval are expected to violate the assumptions of homogeneity or stationarity required for a proper functioning of the eddy covariance technique. An example of an accepted and a rejected ogive is shown in Fig. 4.

The momentum and heat fluxes are treated separately, and two subdatasets are created for the further investigations. In the momentum flux dataset, where only poorly behaved ogives of the cospectral momentum flux estimates were removed from the reference dataset, the number of accepted runs was further reduced to 835 for the ASIT and to 671 for the buoy data. Similarly, only poorly behaved ogives of the cospectral heat flux estimates were removed from the reference dataset, reducing the heat flux dataset to 680 runs for the ASIT data and 609 for the buoy data.
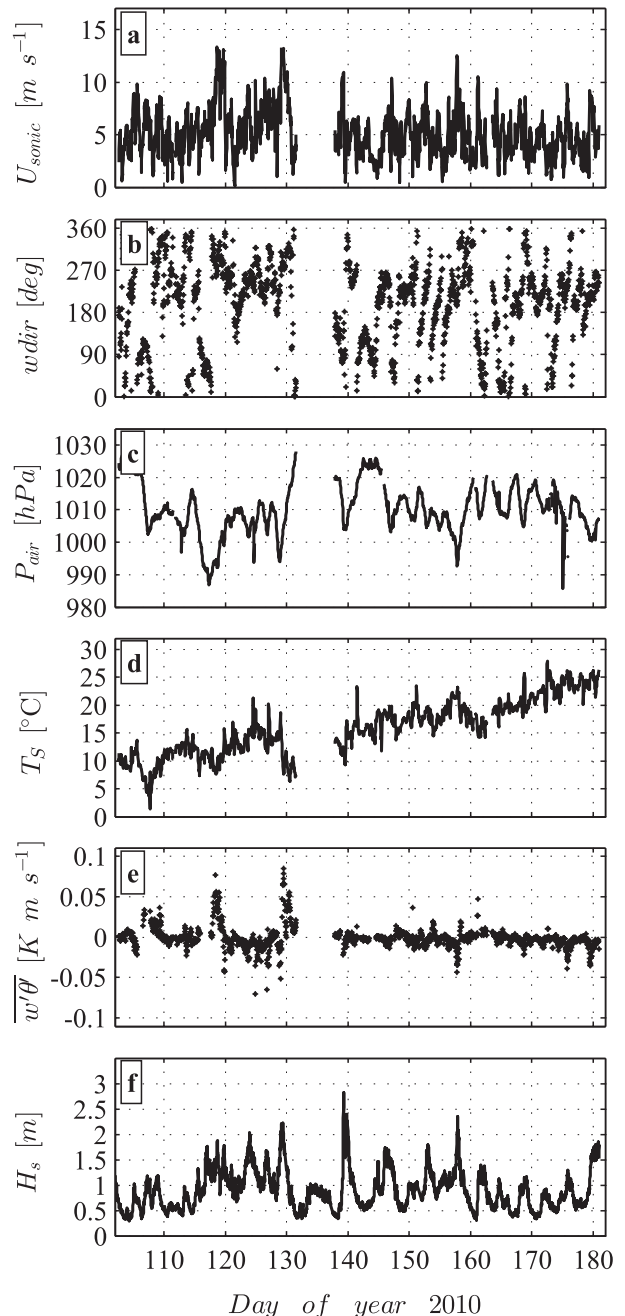

FIG. 3. Overview of the environmental conditions recorded at the ASIT during the course of the field deployment. Time series of (a) wind speed and (b) wind direction from sonic anemometer measurements, (c) air pressure recorded from a pressure sensor mounted at the ASIT, (d) sonic temperature, (e) calculated buoyancy fluxes, and (f) significant wave height recorded at the MVCO's ADCP. No data were recorded between days 131 and 139.

b. Platform motion correction

The motion-corrected wind velocities can be expressed in Earth coordinates as (e.g., Fujitani 1981; Edson et al. 1998)

$$\mathbf{U}_{\text{true}}^{\text{earth}} = \mathbf{T}(\phi, \theta, \psi)[\mathbf{U}_{\text{obs}} + \mathbf{\Omega}_{\text{obs}} \times \mathbf{R}] + \mathbf{V}_{\text{hp}} + \mathbf{V}_{\text{lp}}^{\text{earth}}, \quad (1)$$

where $\mathbf{U}_{\text{true}}^{\text{earth}}$ is the true wind velocity vector relative to the earth, $\mathbf{U}_{\text{obs}}$ denotes the measured wind velocity

vector in the buoy coordinate system, and $\mathbf{T}(\phi, \theta, \psi)$ is the transformation matrix that rotates the platform frame into the reference frame using the Euler angles (ϕ, θ, ψ):

$$\mathbf{T}(\phi,\theta,\psi) = \begin{bmatrix} \cos(\psi)\cos(\theta) & -\sin(\psi)\cos(\phi) + \cos(\psi)\sin(\theta)\sin(\phi) & \sin(\psi)\sin(\phi) + \cos(\psi)\sin(\theta)\cos(\phi) \\ \sin(\psi)\cos(\theta) & \cos(\psi)\cos(\phi) + \sin(\psi)\sin(\theta)\sin(\phi) & \sin(\psi)\sin(\theta)\cos(\phi) - \cos(\psi)\sin(\phi) \\ -\sin(\theta) & \cos(\theta)\sin(\phi) & \cos(\theta)\cos(\phi) \end{bmatrix} \quad (2)$$

Term $\mathbf{\Omega}_{\text{obs}}$ is the angular velocity vector of the platform in the buoy frame, $\mathbf{R}$ denotes the position vector from the IMU to the wind sensor, and $\mathbf{V}_{\text{hp}}$ is the high-pass-filtered wave-induced platform velocity measured by the DCF attitude sensors. These platform velocities are a combination of translational and rotational velocities if the accelerometers are not located at the platform's center of mass. The $\mathbf{\Omega}_{\text{obs}} \times \mathbf{R}$ term accounts for the rotational velocities not sensed by the accelerometers. In Eq. (1), $\mathbf{V}_{\text{lp}}^{\text{earth}}$ is the low-pass-filtered platform velocity relative to the earth.

In this investigation, the platform motions are recorded from accelerometers and angular rate sensors that are strapped down on the buoy, and therefore represent measurements in the platform reference frame. The Euler angles describing the roll ϕ, pitch θ, and yaw ψ are found by a complementary filtering method. As described by Edson et al. (1998), the integrated angular rates $[\int \dot{\phi}(t)\, dt]$ and $[\int \dot{\theta}(t)\, dt]$ are high-pass filtered and are added to the normalized low-pass-filtered accelerometer outputs ($\text{LP}\{\ddot{y}/g\}$ and $\text{LP}\{-\ddot{x}/g\}$) to provide the low-frequency tilts using the small-angle approximation. The most recent version of the algorithm no longer uses the small-angle approximation and estimates the low-frequency contribution instead from $\theta_{\text{lp}} = \text{LP}\{\sin^{-1}[-\ddot{x}/g]\}$ and $\phi_{\text{lp}} = \text{LP}\{\sin^{-1}[-\ddot{y}/g/\cos(\theta_{\text{lp}})]\}$.

The rationale behind this approach is that strapped-down accelerometers, in contrast to those on a gimbaled system, measure a combination of the platform's acceleration and accelerations induced by gravity due to tilting of the platform (Edson et al. 1998; Schulz et al. 2005). Ideally, complementary filtering removes unwanted drift induced by the angular rate sensors while retaining the low-frequency tilts from the accelerometers. A graphical representation of the effects of this method is shown in Fig. 5. It presents the variance spectra of the two time series that are combined to estimate the pitch angle θ, that is, the integrated rate sensors (blue line) and the normalized accelerometers (green line). The individual variance spectra should match over a range of frequencies where the accelerometer is effectively measuring the tilt rather than the linear acceleration of the platform. The

spectra show that this transition occurs for frequencies below approximately $f = 0.1\,\text{Hz}$. The figure also reveals that the spectrum computed from the integrated rate sensor increases at low frequencies due to sensor drift (Schulz et al. 2005). Therefore, a filter is designed by choosing a cutoff frequency that combines the low-frequency tilts from the accelerometer with the high-frequency tilts from the integrated rate sensor to provide accurate estimates of the platform tilts at all frequencies (red line). The choice of the cutoff frequency is discussed further in section 4.

The gravity-induced accelerations are then removed from the accelerometer output in order to compute the wave-induced velocities $\mathbf{V}_{\text{hp}}$ of the measurement platform. The platform velocities are found by applying the coordinate transformation matrix $\mathbf{T}(\phi, \theta, \psi)$ to the accelerometer outputs. This rotates the accelerations into the earth frame, which then allows the removal of the gravitational component from the rotated accelerations. The resulting values are integrated and high-pass filtered to find the platform velocities required in Eq. (1). It should be noted that the use of the accelerometers to estimate the low-frequency component of the angles used in the transformation matrix $\mathbf{T}(\phi, \theta, \psi)$ acts to remove the low-frequency component of the accelerations during the transformation. Therefore, the transformation acts as a high-pass filter prior to integration, and the low-frequency component is removed from $\mathbf{V}_{\text{hp}}$. As a result, this filtering operation is governed by the choice of the cutoff filter frequency f_c used in the complementary filter.

c. Coordinate system and flux calculation

If the platform is changing its position during the measurement (e.g., a cruising ship), then the low-frequency velocity relative to the earth, $\mathbf{V}_{\text{lp}}^{\text{earth}}$, is normally measured by GPS. Alternatively, the true wind velocity relative to water, $\mathbf{V}_{\text{true}}^{\text{water}}$, can be computed by measuring the platform velocity relative to water, $\mathbf{V}_{\text{lp}}^{\text{water}}$, using a current meter. It should be noted that turbulent fluxes are most clearly defined in a reference frame relative to water (see the appendix in Edson et al. 2013). In the present study, measurements were taken from a buoy on an anchored
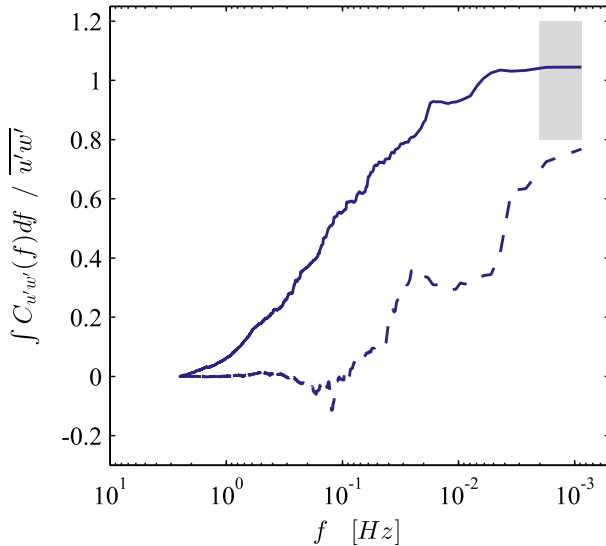
FIG. 4. Example of an accepted (solid line) and rejected (dashed line) ogive of momentum flux cospectral estimates for buoy runs 321 and 153, respectively. The ogives are calculated as a cumulative integral from high to low frequencies and normalized by the magnitude of their corresponding covariances. Accepted ogives approach an asymptotically value of $\int C_{u'w'}(f)\,df/\overline{u'w'} = 1$ inside the ± 0.2 rejection interval at the low-frequency end, which is indicated by the gray-shaded box.
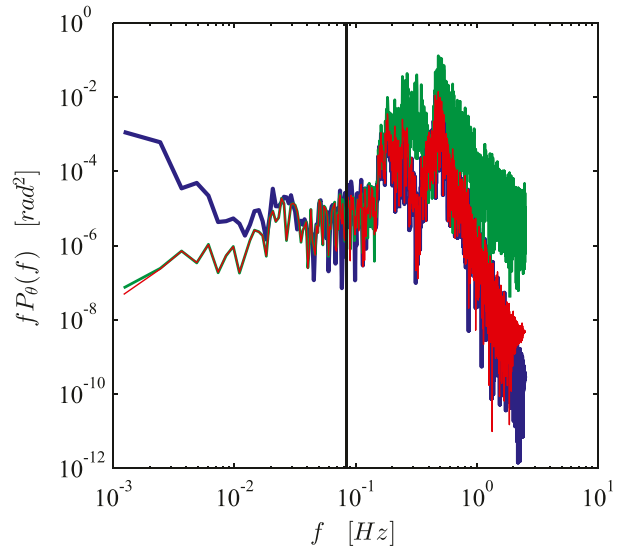
FIG. 5. Pitch angle variance spectra computed from run 321 of the buoy IMU system. The unfiltered pitch spectrum from the integrated angular rate sensor (blue line); the pitch spectrum inferred from the normalized accelerometer output, $-\ddot{x}/g$ (green line); and the spectrum derived by complementary filtering of the integrated angular rate sensor and the normalized accelerometer output (red line). The chosen cutoff frequency ($\tau_c = 12\,\mathrm{s}$) is indicated by the black line.

mooring in shallow water. Although the buoy is free to move relative to its anchor, the longitudinal and lateral velocities due to the buoy watch circle at this depth are small compared to the wind speeds. The last term in Eq. (1) is therefore neglected. Additionally, the use of an earth-relative coordinate system in this study further simplifies the comparison between the buoy-inferred fluxes and those measured from the fixed tower.

The transformation matrix is expected to account for the mean pitch, roll, and yaw of the buoy. Therefore, velocities would be expected to have zero mean tilt after transformation into the local vertical. However, flow distortion over the buoy will cause the streamlines to deviate from the horizontal (Bigorre et al. 2013), inducing an additional tilt to the flow. To account for this, the wind velocities are rotated into the streamwise wind. Such rotation removes the mean lateral and vertical wind components, and the streamwise velocity components become

$$U(t) = \overline{U} + u'(t), V(t) = v'(t), W(t) = w'(t), \quad (3)$$

where the overbar denotes a time-averaged mean and the lowercase letters denote fluctuations around this mean. Therefore, $\overline{U}$ represents the mean streamwise wind speed, while $u'(t)$, $v'(t)$, and $w'(t)$ describe the instantaneous longitudinal (along wind), lateral (crosswind), and vertical

velocity fluctuations, respectively, from this mean streamwise wind.

The rotation of the motion-corrected velocities into the streamwise flow has been shown to reduce the effects of flow distortion (Wyngaard 1981; Oost et al. 1994). However, this approach is most applicable to fixed platforms and at heights well away from the undulated sea surface and the wave-induced flow. Consequently, there remain some uncertainties related to the applicability of this rotation procedure for sensors on a moving platform near the sea surface that will be discussed in section 5.

After applying the correction procedure, the first and last 30 s of every run have been discarded to avoid the Gibbs effect produced by the correction algorithm filters (Weller et al. 2012). Therefore, the fluxes and their associated cospectra are computed using 19-min time series. The remaining motion-corrected time series are then rotated in the streamwise wind as described above and are used to compute the direct covariance fluxes:

$$\overline{w'x'} = \frac{1}{N} \sum_{i=1}^{N} w'_i x'_i, \quad (4)$$

where x' is equal to u', v', or T'_s to compute the kinematic form of the longitudinal and lateral momentum fluxes and the heat flux. The cospectra are computed from the real part of the cross-spectra between these variables.
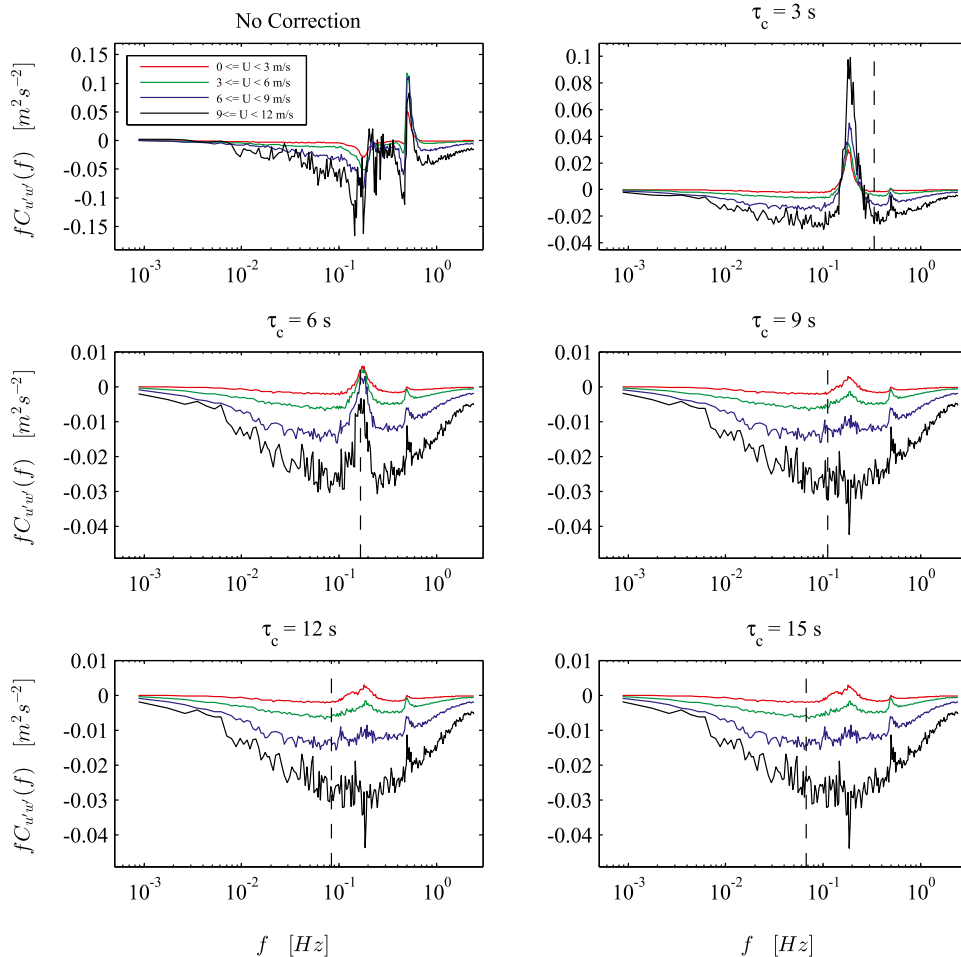
FIG. 6. Cospectral estimates of the momentum flux recorded at the buoy DCF system. The panels show examples of cospectral estimates computed from (upper left) the uncorrected velocities and for the motion-corrected velocities calculated with various cutoff periods between 3 and 15 s. The cospectra have been averaged over the wind speed intervals labeled in the uncorrected subplots. The dashed lines indicate the value of the corresponding cutoff frequency in the subplots.

The temperature variable T'_s represents the sonic temperature fluctuations. The heat flux calculated using the sonic temperature is expected to closely approximate the buoyancy flux (Larsen et al. 1993). The kinematic form of the buoyancy flux is often written as $w'T'_v$, where T'_v represents the virtual temperature fluctuations. As the virtual temperature is closely approximated by the sonic temperature, it allows estimates of the buoyancy flux often needed in studies of near-surface turbulence directly from sonic anemometer measurements (e.g., Edson and Fairall 1998).

4. Results

One of the main goals of this investigation is to optimize the selection of the cutoff frequency for a buoy with a 2.7-m diameter by comparing the motion-corrected measurements with those taken on the ASIT. We can illustrate the impact of the cutoff frequency on the ability to motion correct the buoy data by looking at the behavior of the cospectra over a range of cutoff frequencies (Fig. 6). The cospectra are plotted as a function of the natural frequency in this figure, which facilitates the comparison of the wave-induced motions over the whole range of wind speeds used in the analysis.

a. Impact of the cutoff frequency

The upper-left-hand panel of Fig. 6 shows the uncorrected momentum flux cospectra averaged over the four wind speed bins identified by the labels. The energy-containing subrange is clearly contaminated by

the wave-induced motions, visible as a broad positive peak centered around 0.2 Hz (corresponding to a 5-s wave period). The negative values correspond to an expected downward-directed flux. The magnitude of the contamination increases with wind speed due to the increased magnitude of the heave and the associated increase of the buoy's pitch and roll angles. The co-spectra also show a persistent positive spike at ≈0.5 Hz (i.e., a 2-s period) associated with the resonance frequency of this buoy.

The remaining panels show the results obtained for decreasing cutoff frequencies using the same wind speed bins. The cutoff frequencies are identified by the dashed line in these plots. Even the lowest cutoff period (highest cutoff frequency) is able to remove most of the buoy motion associated with the resonance frequency. However, cospectra generated for the lowest cutoff periods of 3 and 6 s clearly demonstrate that large motion-induced peaks are retained in the wave band. In these cospectra, the cutoff period is set too low and the wave-induced linear accelerations are therefore treated as tilts. As a result, the wave-induced velocities are not removed, and the misinterpreted pitch and roll angles generate a large positive contribution to the cospectra (see Fig. 5).

The wave-induced peak is largely removed at a cutoff period of 9 s and further changes to the cospectra are minimal for increases in the cutoff period beyond 12 s. As the integrated area under the cospectral curve is equal to the measured flux, it is evident from Fig. 6 that the enhanced positive peak in the cospectra computed with $\tau_c \leq 6$ s ($f_c \geq 0.17$ Hz) will lead to reduced magnitudes of the atmosphere-to-ocean momentum flux compared to cospectra computed with a cutoff frequency beyond the wave band. However, the positive contribution to the cospectra is still noticeable in the corrected spectra, particularly at the lowest wind speed range. Whether this contribution is real or an artifact of the motion-correction procedure is further discussed in section 5.

b. Selection of the cutoff frequency

The ability to properly motion correct the velocity measurements with the method presented in this study is clearly sensitive to the choice of the cutoff frequency. One objective method for the determination of an appropriate value is to investigate how the root-mean-square (RMS) difference between the ASIT and buoy estimates of the momentum flux changes with increasing values of the cutoff period. The corresponding results are shown in Fig. 7. The dashed line in this figure indicates the RMS difference between the ASIT and the uncorrected buoy data.
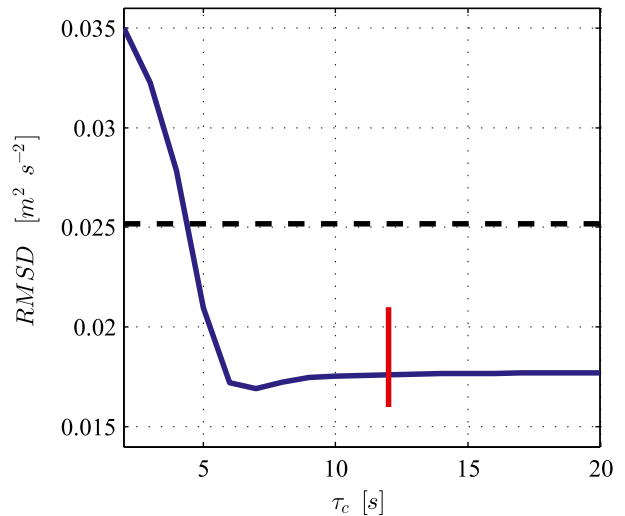

FIG. 7. The RMS difference of the momentum fluxes recorded at the ASIT and buoy as a function of the cutoff period. The dashed line represents the RMS difference between the ASIT and the uncorrected buoy fluxes. The red line represents the cutoff period chosen for the remaining analysis.

The results show that the use of cutoff periods shorter than 4 s distinctly increases the uncertainty. This is in agreement with the results presented in Fig. 6 and confirms that the treatment of accelerations in the wave band as tilts introduces noise into the cospectra. The RMS differences rapidly fall to a weak minimum at $\tau_c = 7$ s before slightly increasing again and leveling out at a value of around 12 s. As the corresponding cospectra for $\tau_c = 6$ s still contain considerable distortions, we have decided to use a somewhat larger value of $\tau_c = 12$ s in our analysis. For this cutoff period the disturbances in the flux estimates are substantially reduced. We believe that this value provides a good compromise for the calculation of the motion-corrected flux estimates over a wider range of sea states for the type of research buoy used in this study.

c. Momentum and heat fluxes

To investigate the overall improvement of the buoy measurements as a result of the applied motion correction, both uncorrected and motion-corrected estimates of the buoy's momentum and buoyancy fluxes are compared against the ASIT measurements. The motion-correction algorithm uses the recommended value of the cutoff period, $\tau_c = 12$ s, and the fluxes are averaged over 19 min. Figure 8 shows a comparison between the momentum fluxes ($-\rho\overline{u'w'}$) from the buoy and the ASIT before and after the motion correction. Without motion correction, the magnitudes of the momentum fluxes recorded at the buoy are slightly overestimated compared
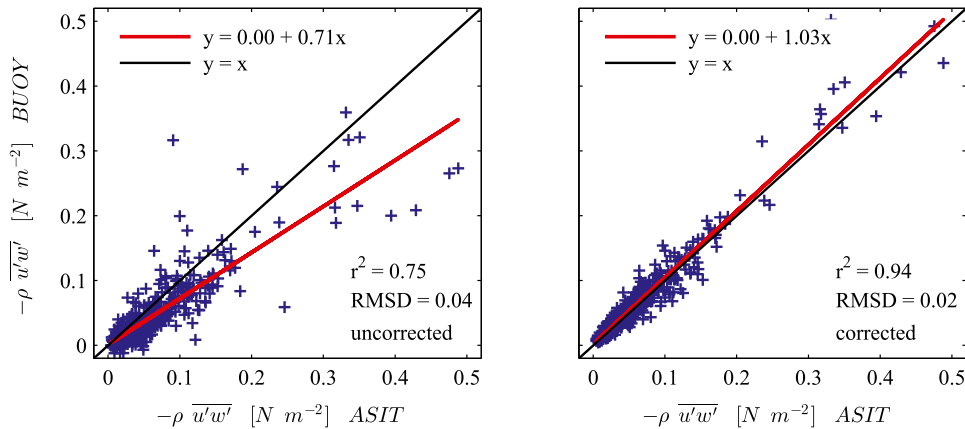
FIG. 8. A comparison of (left) uncorrected and (right) motion-corrected momentum flux estimates recorded at the ASIT and the buoy DCF system. Only data with availability from both DCF systems during the measurement period (12 Apr–29 Jun 2010) are shown. The data represent runs averaged over 19 min and are limited to winds blowing from 165° to 345°. The coefficients of the regression line and the total sample variance explained by the linear regression are given in the respective panels.

to those recorded at the ASIT. Correcting the buoy data for the wave-induced platform velocities reduces the RMS difference distinctly by 50% and increases the total sample variance, r^2, explained by the linear regression between the buoy and the ASIT estimates, from 0.75 to 0.94. Edson et al. (1998) and Miller et al. (2008) concluded that motion-corrected fluxes performed from research vessels overestimate momentum fluxes by approximately 15%, primarily due to flow distortion. The magnitude of the flux overestimation depends on both the location of the DCF sensors and the deflection of the streamlines around the ship. The good

agreement between the motion-corrected flux estimates and those of the ASIT in Fig. 8 suggests that the flow distortion is minimized for the type of buoy used in this study.

A corresponding comparison of the uncorrected and corrected heat fluxes $\rho C_p \overline{w'T'_s}$, where C_p is the specific heat at constant pressure, is presented in Fig. 9. Compared to the momentum fluxes, the uncorrected buoyancy fluxes show a higher correlation. This is expected for scalar fluxes, since the temperature fluctuations are less sensitive to buoy motions than the horizontal velocity. Nevertheless, the motion correction also clearly
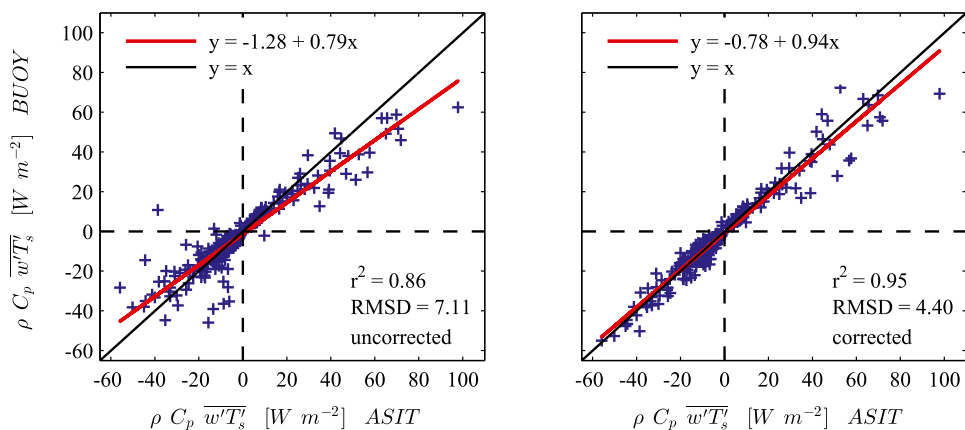

FIG. 9. A comparison of (left) uncorrected and (right) motion-corrected sonic temperature (buoyancy) flux estimates recorded at the ASIT and the buoy DCF system. Only data with availability from both DCF systems during the measurement period (12 Apr–29 Jun 2010) are shown. The data represent runs averaged over 19 min and are limited to winds blowing from 165° to 345°. The coefficients of the regression line and the total sample variance explained by the linear regression are given in the respective panels.
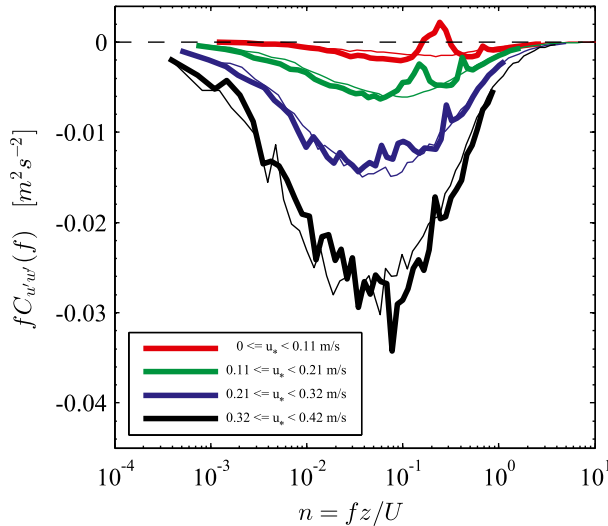
FIG. 10. Cospectral estimates of the momentum flux as a function of the normalized frequency. The cospectra are bin averaged by u_* as indicated by the legend. The thick lines represent the motion-corrected buoy data, and the thin lines represent the ASIT data.

FIG. 11. Cospectral estimates of the sonic temperature (buoyancy) flux as a function of normalized frequency. The cospectra have been normalized by u_* and bin averaged by T_* as indicated by the legend. The thick lines represent the motion-corrected buoy data, and the thin lines represent the ASIT data.

improves the results for the buoyancy flux both with respect to the slope of the linear regression from 0.79 to 0.94 and the explained variance from 0.86 to 0.95.

d. Momentum and heat cospectra

Frequency-weighted ensemble-averaged cospectra of the vertical momentum, $fC_{u'w'}(f)$, and heat flux, $fC_{w'T_s'}(f)$, are shown in Figs. 10 and 11. The momentum fluxes shown in Fig. 10 have been bin averaged with respect to the friction velocity u_* rather than the wind speed, to account for the effects of atmospheric stability. However, the bin intervals for the friction velocity were chosen using the linear relationship $u_* = 0.035 U_N$. Therefore, the four selected wind speed bins correspond to neutral wind speeds between 0 and $3\,\mathrm{m\,s^{-1}}$ (red lines), 3 and $6\,\mathrm{m\,s^{-1}}$ (green lines), 6 and $9\,\mathrm{m\,s^{-1}}$ (blue lines), and 9 and $12\,\mathrm{m\,s^{-1}}$ (black lines). It is worth noting that the 5-Hz sampling frequency used on the buoy system does not capture all the high-frequency components of the flux at the higher wind speed; that is, the curve of the cospectra approaches but does not reach zero at the Nyquist frequency of 2.5 Hz. The 20-Hz sampling rate (or a Nyquist frequency of 10 Hz) used with the ASIT system is sufficient, at least for the investigated range of wind speeds, and the sampling frequency for the buoy system should be increased to this value for future studies.

The ASIT and buoy cospectra are in reasonably good agreement. However, the momentum flux cospectra of the buoy clearly show a peak at the frequency range of
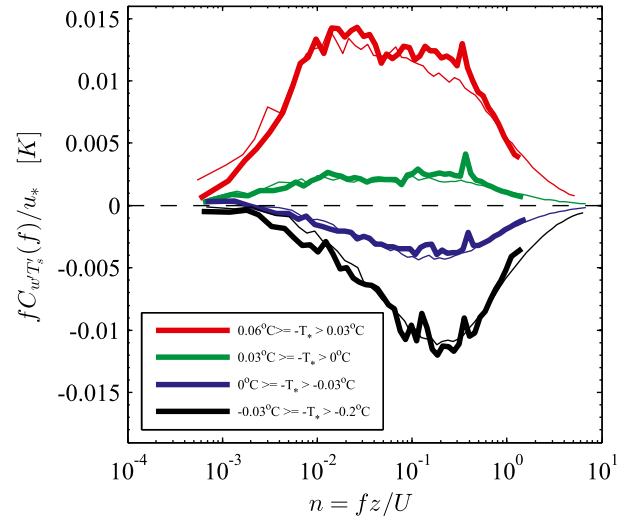
the underlying wave field for wind speeds below $8\,\mathrm{m\,s^{-1}}$, while no peak is identified in the ASIT cospectra. The interpretation of these results is complicated by the fact that the buoy measurements are essentially made in a wave-following coordinate system, while the tower measurements are made relative to the fixed earth coordinate system over a nonstationary wave–influenced surface. One might expect the cospectra measured in these two coordinate systems to differ, especially close to the ocean surface. In fact, the expected shape and behavior of the cospectra for measurements in the wave-following reference frame is even qualitatively unclear, as corresponding previous studies (e.g., Kaimal et al. 1972; Wyngaard and Coté 1972; Højstrup 1982) have mainly been performed over land and are therefore based on fixed measurements where the mean height about the surface was unambiguous. Additionally, most spectral theory is based on wavenumber spectra and the use of the relationship $k = 2\pi f/\overline{U}$ given by Taylor's frozen turbulence hypothesis to convert between frequency and wavenumber spectra, where k is the wavenumber and $\overline{U}$ is the mean streamwise velocity in Eq. (3). The validity of the frozen turbulence hypothesis for a moving platform near the wavy ocean surface might also be questionable.

A closer look at the observations in this study indicates that the wave-induced peaks in the buoy's cospectra are limited to light winds over old seas. A comparison of the buoy and ASIT momentum flux cospectra, sorted according to wind speed and wave age,
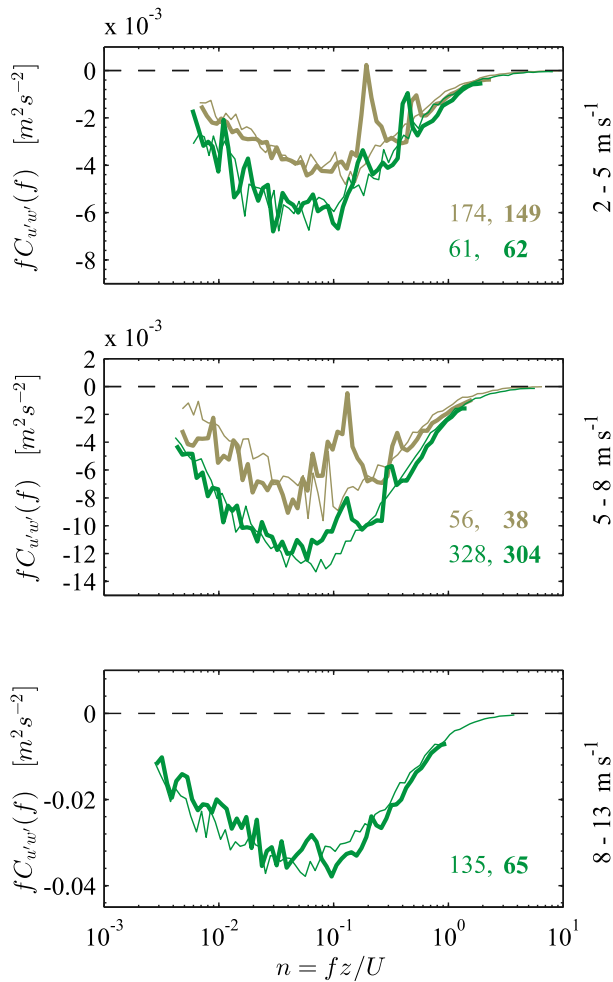
FIG. 12. Cospectral estimates of the momentum flux as function of normalized frequency. The cospectra are bin averaged by the wave age parameter: $40 \leq c_p/u_* < 70$ (old decaying seas, i.e., swell; brown line) and $10 \leq c_p/u_* < 40$ (developing and fully developed sea; green line). The thick lines represent the motion-corrected buoy data, and the thin lines represent the ASIT data. The number of averaged spectra is given in each panel.

c_p/u_*, is shown in Fig. 12. For fully developed and developing seas (green lines), both the buoy and ASIT cospectra are in good agreement, regardless of the wind speed. For wind speeds below $5 \, \mathrm{m \, s^{-1}}$, the majority of the recorded runs are associated with old seas, that is, swell conditions (brown lines). The analysis of both datasets revealed that approximately 20% of the buoy runs are associated with a peak in the momentum flux cospectra at low wind speeds and old seas. Therefore, the bulk of the buoy's momentum flux cospectra are found to be in good agreement with the ASIT cospectra even during low wind speeds and swell conditions. The integration of the motion-corrected momentum flux cospectra, which are contaminated by a peak in the

frequency range of the waves, produces flux estimates that are found to be in good agreement with those of the ASIT, as shown in section 4c. This indicates that the cospectral behavior of the momentum flux may suffer from some of the issues described above, while the point-by-point covariance between the vertical and horizontal velocity fluctuations seems to be less affected.

The corresponding buoyancy flux cospectra are shown in Fig. 11. The cospectra in this figure have been normalized by the friction velocity u_* to remove the wind speed dependency and bin averaged by the temperature scaling parameter $T_* = -\overline{w'T_s'}/u_*$. The ranges in Fig. 11 are given by $-T_*$ such that the positive ranges are associated with upward fluxes and unstable conditions and negative ranges with downward fluxes and stable conditions. After removal of the wave-induced platform velocities in the anemometer measurements, the corrected cospectra are in good agreement with those observed at the ASIT. The buoy cospectra in Fig. 11 still retain the small peak at $n \approx 0.3$, which corresponds to the buoy's resonance frequency ($f \approx 0.5 \, \mathrm{Hz}$). However, Fig. 9 clearly shows that the motion-corrected point-to-point buoyancy fluxes are in good agreement with those recorded at the ASIT. We are confident that the error in the flux contribution due to this peak is small and therefore negligible.

e. Wave statistics

This section investigates how well wave-related parameters, such as significant wave height, wave direction, and the wave peak period, can be measured from the type of buoy used here. A common method to measure waves from a fixed subsurface platform is the PUV approach (Nagata 1964). This technique originally involves simultaneous high-frequency measurements of water pressure (P) and horizontal ocean current velocities (U, V) at a fixed depth below the sea surface. These measurements can then be used to compute surface elevation spectra of both current velocity and pressure, from which wave-related parameters such as significant wave height and wave direction can be determined.

Measurements of water pressure at a constant depth are generally difficult to obtain from a floating platform. Instead, we have adapted an approach developed by Gordon and Lohrmann (2001), where we use the buoy's linear velocities and heave (rather than pressure) calculated at its center of mass. This is accomplished by adjusting the position vector **R** in Eq. (1) to represent the distance between the motion sensors and the center of mass. Additionally, the filter cutoff period is increased to $\tau_c = 40 \, \mathrm{s}$ to give better estimates of the wave

field at low frequencies. The heave (i.e., the vertical displacement relative to the mean seawater level) is found by integration and high-pass filtering of the vertical velocity component of Eq. (1).

Applying the modified PUV approach, the heave and velocity variance spectra are combined with the cross-spectra between the heave and the velocity components to compute directional wave spectra (Gordon and Lohrmann 2001). However, in contrast to the original PUV approach, where wave velocity and pressure are recorded below the sea surface, these spectra are already obtained for the ocean surface (surface elevation spectra) and do not need to be depth corrected. Integration over the heave variance spectra provides the standard deviation of the sea surface elevation. It also provides an estimate for the significant wave height, which is defined as 4 times the standard deviation. The direction of the waves at the peak of the heave spectrum is estimated from the two cross-spectra by taking the four-quadrant inverse tangent. The peak period is determined from the maximum value of the heave spectrum, while the average wave period is found from an approach known as "zero crossing" (e.g., Cartwright and Longuet-Higgins 1956). The wave periods can be used with the wave equation to determine the phase speed and the wavelength.

Time series of wave statistics computed from this approach are compared with data from the MVCO ADCP in Fig. 13. The ADCP was located at a water depth of 12 m and at a distance of approximately 1 km from the buoy. The ADCP data were recorded at discrete frequencies, and the data were smoothed by a moving average over 11 data points prior to the data comparison. Both the significant wave height and the wave direction computed from the ADCP and the buoy data are found to be in reasonable agreement (Figs. 13a and 13b). The corresponding scatterplots in Figs. 14a and 14b show that the significant wave height can be estimated from the buoy's heave with a high degree of certainty, while buoy estimates of the wave direction, derived from the modified PUV approach, are found to be slightly overestimated compared to the ADCP measurements. The offset between the two measurements platforms were on average found to be in the range of 10°–20°. Time series of the mean wave period, the phase speed, and the wavelength are compared with ADCP data in Figs. 13c–e. The corresponding scatterplots are shown in Figs. 14c–e. It is evident that the estimates from the modified PUV approach are underestimated compared to those of the ADCP. The offset between the buoy and ADCP estimates of the mean wave period and the phase speed are both on the order of $1 \, \mathrm{m \, s^{-1}}$. The difference between the
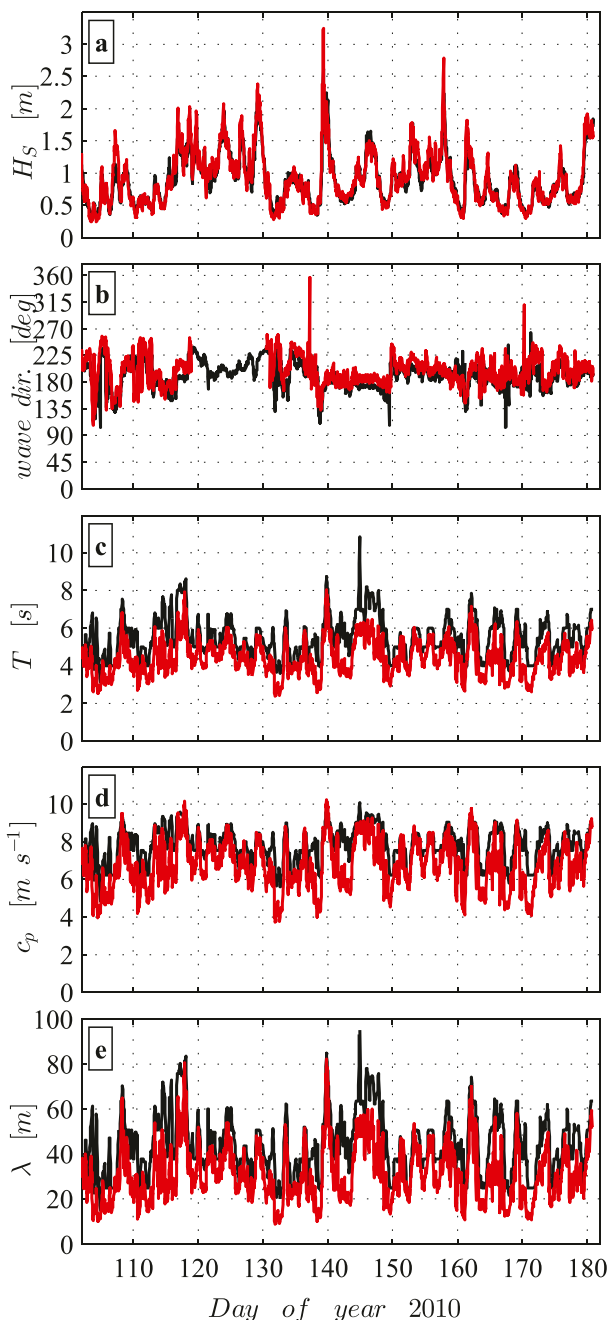

FIG. 13. Wave statistics computed from the buoy data (red) compared with data from the MVCO ADCP (black). The ADCP was located at a water depth of 12 m at a distance of approximately 1 km from the buoy. Panels showing (a) significant wave height, (b) wave direction at the peak of the spectrum, (c) wave phase speed, (d) mean wave period, and (e) wavelength. Data for wave direction between days 119 and 131 are removed due to a malfunction in the buoy's compass and the associated inaccurate estimation of the PUV cross-spectra.
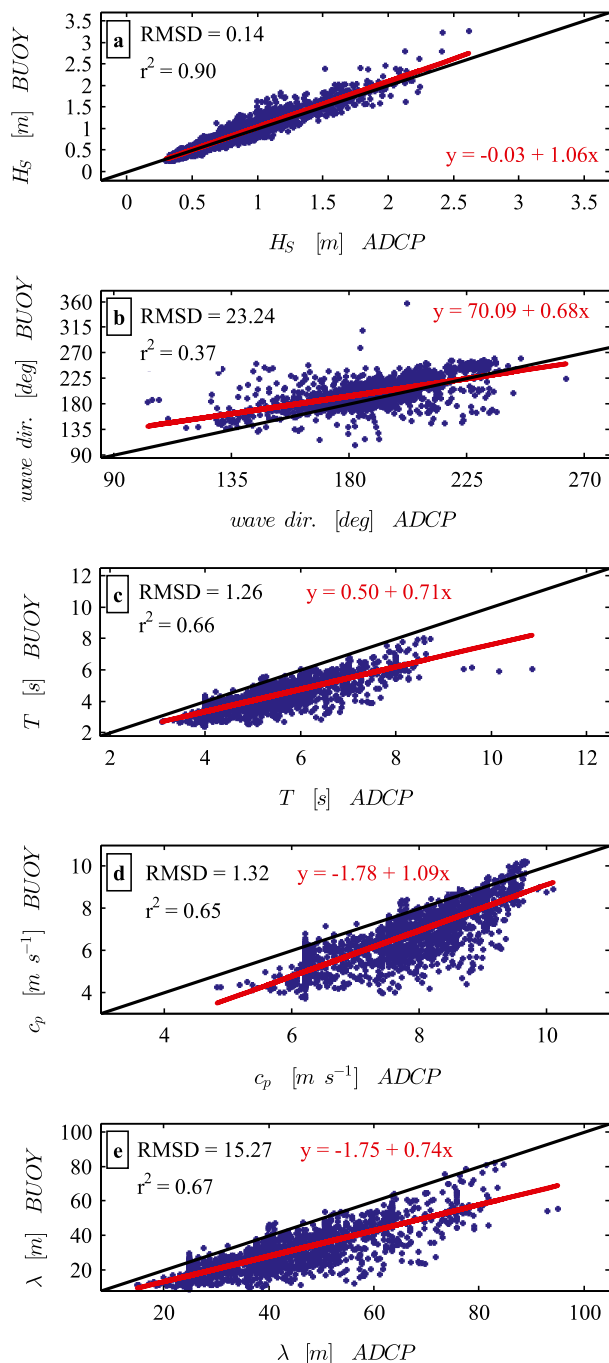
FIG. 14. Scatterplots of wave statistics derived from the buoy and ADCP time series shown in Fig. 13. Panels showing (a) significant wave height, (b) wave direction at the peak of the spectrum, (c) mean wave period, (d) wave phase speed, and (e) wavelength. The coefficients of the regression line (red lines) and the total sample variance explained by linear regression are given in the respective panels; $x = y$ (black lines).

estimates of the wavelength is typically found to be in the range of 10–15 m.

We speculate that the differences in the wave statistics between the buoy (based on the PUV estimates) and the ADCP data are mainly due to the design of these two measurement platforms. While the ADCP is a stationary (nonmoving) instrument specially designed to observe ocean currents and the wave field, the buoy used in this study was not designed for this specific purpose. For example, estimation of the wave direction (Figs. 13b and 14b) by the modified PUV approach relies upon the buoy's horizontal motions at the center of its mass. Since the buoy is moored, it can only move with the surface currents within the radius of its watch circle. Moreover, the mooring is exposed to the wind, which has the ability to slightly influence its current-induced drift. Therefore, the horizontal velocities used to compute the heave–velocity cross-spectra might be biased and thus result in erroneous PUV estimates of the wave direction. Despite the discrepancies in Figs. 13b and 14b, we are confident that the modified PUV approach can provide a crude estimate of the wave direction in conditions where the surface currents, resulting from the predominant wind field, and the predominant wave directions are mostly aligned, which was mainly observed in the present study. Another limitation to the modified PUV approach is the diameter of the buoy. The time series of the wave phase speed and the wavelength (Figs. 13d and 13e) were derived from the mean wave period (zero crossing), which is highly dependent on the minimum wavelength that can be resolved by the buoy. The minimum resolution will be at least double the buoy's diameter (i.e., approximately 5.5 m). Therefore, the discrepancies between the buoy and ADCP data in Figs. 13d and 13e and 14d and 14e might be due to the limited resolution in the mean wave period measurements, in addition to uncertainties in the estimation of the wave period (Bakhoday-Paskyabi and Fer 2014). Nevertheless, the time series from the buoy are in reasonable agreement with those of the ADCP. This suggests that the surface mooring used in this study has the ability to record basic wave statistics of reasonable quality by use of its accelerometer data and the modified PUV approach.

5. Discussion and summary

In this study, DCF measurements of momentum and buoyancy fluxes in the marine atmospheric boundary layer have been determined from a surface buoy and from the Air–Sea Interaction Tower (ASIT) at the Martha's Vineyard Coastal Observatory (MVCO) between April and June 2010. A DCF system was mounted on the MVCO's ASIT, which is located 3.2 km offshore

in a water depth of 15 m. The buoy was equipped with a similar system and was moored approximately 500 m southwest of the ASIT. Using a motion-correction algorithm based on Edson et al. (1998), sonic anemometer measurements recorded at the buoy have been corrected for wave-induced platform motions.

The ability of the motion-correction algorithm to filter out wave-induced platform motions from the sonic anemometer data has been shown in earlier publications, such as Fairall et al. (1997) and Miller et al. (2008). However, these studies compared only motion-corrected flux measurements between floating platforms (e.g., ship or buoy). The performance of the correction algorithm has not yet been investigated by comparison between a floating platform and a fixed structure, such as an offshore tower.

Buoys have advantages for long-term investigation of air–sea interaction processes as they can easily be deployed in remote areas of the world oceans. Equipped with both oceanographic and meteorological sensors, these platforms provide researchers with data needed for ocean, weather, and climate research. As the heat and momentum flux across the air–sea interface have a profound impact on both the ocean and atmosphere, it is natural to equip buoys with DCF systems to improve our understanding of the turbulent exchange processes. Therefore, an investigation of the feasibility of DCF measurements from small floating platforms is highly needed.

The comparison of the heat and momentum fluxes and cospectra shows that DCF measurements in the MABL can be performed with nearly the same accuracy from buoys as from fixed towers when the wave-induced platform motions are removed from the wind measurements. After correction for platform motions, the momentum fluxes of both systems show an r^2 of 0.94 and an RMS difference of $0.02 \, \text{N m}^{-2}$. The corresponding values for the buoyancy fluxes are 0.95 and $4.40 \, \text{W m}^{-2}$.

The flux measurements from the ASIT allowed a systematic investigation of the cutoff frequency used in the buoy motion-correction algorithm under various atmospheric and sea-state conditions. The choice of the cutoff period depends on the frequency of the platform motion and thus on both the wave state and the individual platform characteristics. Based on the comparisons between the type of buoy used in this study and the ASIT, we recommend a cutoff period of $\tau_c = 12 \, \text{s}$ that will be suitable in most wind and wave conditions. However, there are still several outstanding issues that could be addressed to improve the method. Specifically, the velocity measurements made on a surface buoy differ from those made on a fixed

platform. The buoy measurements are essentially made in a wave-following coordinate system, while the tower measurements are made relative to Earth. This causes uncertainty on how to interpret fluxes made in either coordinate system.

For example, measurements from fixed platforms (e.g., Hristov et al. 2003) show clear wave-induced fluctuations in the measured velocities that cause enhanced variance in the autospectra. The correlation between these fluctuations is associated with a wave-induced component of the momentum flux at the height of measurement. However, the wave-induced flux is expected to be negligible above the wave boundary layer (WBL). While the height of the WBL is not universally defined (e.g., Edson et al. 2013), it is typically assumed to be in the order of the significant wave height. This is demonstrated by the lack of a wave-induced peak in the ASIT cospectra. However, there remains some uncertainty in how to remove the wave-induced platform motion in the buoy coordinate system.

It is of interest to determine the cause of the peak in the buoy-derived cospectral estimates for low wind speeds (Fig. 12) to reduce the uncertainty of the fluxes under light wind conditions. One hypothesis for the observed behavior is related to the expected flow in light winds over swell. The streamlines in this case are expected to follow these long waves near the surface. The wave-induced flow should then decay exponentially with height and become quasi-horizontal at heights where measurements are typically made aboard ships. A sonic anemometer mounted above the wave-induced flow will move relative to the streamlines. Therefore, the ship's heave motions will be clearly visible in the uncorrected wind measurements. On the other hand, an anemometer mounted on a buoy moving with the wave-following streamlines can be expected to see less motion relative to these streamlines. As a result, the motion-correction algorithm may be correcting for a wave-induced vertical velocity of these longer waves (i.e., heave) that is not apparent in the uncorrected anemometer measurements of the buoy. We hypothesize that this induces a wave-correlated signal in the motion-corrected vertical velocity component that could lead to the observed peak in the cospectra.

However, this hypothesis fails when the streamlines are not surface following. Analysis of the sonic anemometer data from both datasets reveal that the wind speeds measured at the ASIT are 2% lower than those recorded at the buoy, and that the difference in the measured wind speed between the buoy's ASIMET sensors and the 3D sonic anemometer never exceeded 5% (Bigorre et al. 2013). As these differences are within the accuracy of the sensors, and finding reasonably good

agreement between the ASIT and motion-corrected buoy momentum and buoyancy fluxes, we are confident that the flow distortion at the buoy sensors is minimal. Nonetheless, we cannot dismiss the possibility that the observed peak in the cospectral estimates is induced by flow distortion over the buoy hull or the instrumentation, which becomes noticeable in the cospectra in conditions of light winds and swell. A more detailed investigation of the flow characteristics from both ASIT and the buoy would be required to identify this issue (e.g., Landwehr et al. 2015; Prytherch et al. 2015). This is, however, beyond the scope of this paper.

If the buoy anemometer is generally in a coordinate system following the flow, then noise may be added by removing the low-frequency platform velocities that are not actually part of the measured wind velocities. Our results show that this is mainly a problem in light winds over swell, that is, old seas. In fact, the range of frequencies over which a peak is found in the cospectra shown in Fig. 12 widens when a lower cutoff frequency is chosen. We therefore speculate that the peak in the buoy's cospectra is an artifact of the motion-correction itself and mainly occurs in the presence of light winds and swell. Methods are being developed both to test and to potentially correct for this effect in the future.

A possible solution to address this potential limitation in the correction algorithm is to dynamically adjust the cutoff frequency to a higher value based on wind and wave parameters. This requires a means to choose the value of the cutoff frequency based on, for example, wave age or wave slope. Another approach is to look into possibilities to remove the correlation between the heave and motion-corrected vertical velocity (e.g., Miller et al. 2010; Edson et al. 2011; Blomquist et al. 2014; Prytherch et al. 2015). We are actively investigating this and other approaches in ongoing investigations.

REFERENCES

Anctil, F., M. A. Donelan, W. M. Drennan, and H. C. Graber, 1994: Eddy-correlation measurements of air–sea fluxes from a discus buoy. *J. Atmos. Oceanic Technol.*, **11**, 1144–1150, doi:10.1175/1520-0426(1994)011<1144:ECMOAS>2.0.CO;2.

Austin, T. C., and Coauthors, 2002: A network-based telemetry architecture developed for the Martha's Vineyard Coastal Observatory. *IEEE J. Oceanic Eng.*, **27**, 228–234, doi:10.1109/JOE.2002.1002477.

Bakhoday-Paskyabi, M., and I. Fer, 2014: The influence of surface gravity waves on the injection of turbulence in the upper ocean. *Nonlinear Processes Geophys.*, **21**, 713–733, doi:10.5194/npg-21-713-2014.

Bigorre, S. P., R. A. Weller, J. B. Edson, and J. D. Ware, 2013: A surface mooring for air–sea interaction research in the Gulf Stream. Part II: Analysis of the observations and their accuracies. *J. Atmos. Oceanic Technol.*, **30**, 450–469, doi:10.1175/JTECH-D-12-00078.1.

Blomquist, B. W., B. J. Huebert, C. W. Fairall, L. Bariteau, J. B. Edson, J. E. Hare, and W. R. McGillis, 2014: Advances in air-sea flux measurement by eddy correlation. *Bound.-Layer Meteor.*, **152**, 245–276, doi:10.1007/s10546-014-9926-2.

Cartwright, D. E., and M. S. Longuet-Higgins, 1956: The statistical distribution of the maxima of a random process. *Proc. Roy. Soc. London*, **237A**, 212–232, doi:10.1098/rspa.1956.0173.

Colbo, K., and R. A. Weller, 2009: Accuracy of the IMET sensor package in the subtropics. *J. Atmos. Oceanic Technol.*, **26**, 1867–1890, doi:10.1175/2009JTECHO667.1.

Crawford, T. L., R. T. McMillen, T. P. Meyers, and B. B. Hicks, 1993: Spatial and temporal variability of heat, water, vapor, carbon dioxide, and momentum air-sea exchange in a coastal environment. *J. Geophys. Res.*, **98**, 12 869–12 880, doi:10.1029/93JD00628.

Crofoot, R. F., 2004: Investigations of scalar transfer coefficients in fog during the Coupled Boundary Layers and Air-Sea Transfer Experiment: A case study. M.S. thesis, Dept. of Ocean Engineering, Massachusetts Institute of Technology, and Woods Hole Oceanographic Institution, 72 pp., doi:10.1575/1912/2065.

Dugan, J. P., S. L. Panichas, and R. L. Dimarco, 1991: Decontamination of wind measurements from buoys subject to motions in a seaway. *J. Atmos. Oceanic Technol.*, **8**, 85–95, doi:10.1175/1520-0426(1991)008<0085:DOWMFB>2.0.CO;2.

Dunckel, M., L. Hasse, L. Krügermeyer, D. Schrievers, and J. Wucknitz, 1974: Turbulent fluxes of momentum, heat and water vapor in the atmospheric surface layer at sea during ATEX. *Bound.-Layer Meteor.*, **6**, 81–106, doi:10.1007/BF00232478.

Edson, J. B., and C. W. Fairall, 1998: Similarity relationships in the marine atmospheric surface layer for terms in the TKE and scalar variance budgets. *J. Atmos. Sci.*, **55**, 2311–2328, doi:10.1175/1520-0469(1998)055<2311:SRITMA>2.0.CO;2.

——, A. A. Hinton, K. E. Prada, J. E. Hare, and C. W. Fairall, 1998: Direct covariance flux estimates from mobile platforms at sea.

J. Atmos. Oceanic Technol., **15**, 547–562, doi:10.1175/1520-0426(1998)015<0547:DCFEFM>2.0.CO;2.

——, C. J. Zappa, J. A. Ware, W. R. McGillis, and J. E. Hare, 2004: Scalar flux profile relationships over the open ocean. *J. Geophys. Res.*, **109**, C08S09, doi:10.1029/2003JC001960.

——, and Coauthors, 2007: The Coupled Boundary Layers and Air–Sea Transfer Experiment in low winds. *Bull. Amer. Meteor. Soc.*, **88**, 341–356, doi:10.1175/BAMS-88-3-341.

——, and Coauthors, 2011: Direct covariance measurement of CO_2 gas transfer velocity during the 2008 Southern Ocean Gas Exchange Experiment: Wind speed dependency. *J. Geophys. Res.*, **116**, C00F10, doi:10.1029/2011JC007022.

——, and Coauthors, 2013: On the exchange of momentum over the open ocean. *J. Phys. Oceanogr.*, **43**, 1589–1610, doi:10.1175/JPO-D-12-0173.1.

Fairall, C. W., E. F. Bradley, D. P. Rogers, J. B. Edson, and G. S. Young, 1996: Bulk parameterization of air-sea fluxes for Tropical Ocean-Global Atmosphere Coupled-Ocean Atmosphere Response Experiment. *J. Geophys. Res.*, **101**, 3747–3764, doi:10.1029/95JC03205.

——, A. B. White, J. B. Edson, and J. E. Hare, 1997: Integrated shipboard measurements of the marine boundary layer. *J. Atmos. Oceanic Technol.*, **14**, 338–359, doi:10.1175/1520-0426(1997)014<0338:ISMOTM>2.0.CO;2.

Farrar, J. T., and Coauthors, 2015: Salinity and temperature balances at the SPURS central mooring during fall and winter. *Oceanography*, **28** (1), 56–65, doi:10.5670/oceanog.2015.06.

Fischer, G., 2006: Installation and operation of the research platform FINO 1 in the North Sea. *Offshore Wind Energy: Research on Enviromental Impacts*, D. J. Köller, J. Köppel, W. Peters, Eds., Springer, 237–253, doi:10.1007/978-3-540-34677-7_15.

Fujitani, T., 1981: Direct measurements of turbulent fluxes over the sea during AMTEX. *Pap. Meteor. Geophys.*, **32**, 119–134, doi:10.2467/mripapers.32.119.

——, 1985: Method of turbulent flux measurement on a ship by using a stable platform system. *Pap. Meteor. Geophys.*, **36**, 157–170, doi:10.2467/mripapers.36.157.

Gordon, L., and A. Lohrmann, 2001: Near-shore Doppler current meter wave spectra. *Ocean Wave Measurement and Analysis: Proceedings of the Fourth International Symposium*, B. L. Edge and J. M. Hemsley, Eds., Vol. 1, American Society of Civil Engineers, 33–43, doi:10.1061/40604(273)4.

Högström, U., and Coauthors, 2008: Momentum fluxes and wind gradients in the marine boundary layer—A multi-platform study. *Boreal Environ. Res.*, **13**, 475–502.

Højstrup, J., 1982: Velocity spectral in the unstable planetary boundary layer. *J. Atmos. Sci.*, **39**, 2239–2248, doi:10.1175/1520-0469(1982)039<2239:VSITUP>2.0.CO;2.

Hosom, D. S., R. A. Weller, R. E. Payne, and K. E. Prada, 1995: The IMET (improved meteorology) ship and buoy systems. *J. Atmos. Oceanic Technol.*, **12**, 527–540, doi:10.1175/1520-0426(1995)012<0527:TIMSAB>2.0.CO;2.

Hristov, T. S., S. D. Miller, and C. A. Friehe, 2003: Dynamical coupling of wind and ocean waves through wave-induced air flow. *Nature*, **422**, 55–58, doi:10.1038/nature01382.

Kaimal, J., J. C. Wyngaard, Y. Izumi, and O. R. Cote, 1972: Spectral characteristics of surface-layer turbulence. *Quart. J. Roy. Meteor. Soc.*, **98**, 563–589, doi:10.1002/qj.49709841707.

Landwehr, S., N. O'Sullivan, and B. Ward, 2015: Direct flux measurements from mobile platforms at sea: Motion and airflow distortion corrections revisited. *J. Atmos. Oceanic Technol.*, **32**, 1163–1178, doi:10.1175/JTECH-D-14-00137.1.

Larsen, S. E., J. B. Edson, C. W. Fairall, and P. G. Mestayer, 1993: Measurement of temperature spectra by a sonic anemometer. *J. Atmos. Oceanic Technol.*, **10**, 345–354, doi:10.1175/1520-0426(1993)010<0345:MOTSBA>2.0.CO;2.

Liu, W. T., K. B. Katsaros, and J. A. Businger, 1979: Bulk parameterization of air-sea exchanges of heat and water vapor including the molecular constraints at the interface. *J. Atmos. Sci.*, **36**, 1722–1735, doi:10.1175/1520-0469(1979)036<1722:BPOASE>2.0.CO;2.

Marshall, J., and Coauthors, 2009: The CLIMODE field campaign: Observing the cycle of convection and restratification over the Gulf Stream. *Bull. Amer. Meteor. Soc.*, **90**, 1337–1350, doi:10.1175/2009BAMS2706.1.

Miller, S. D., T. S. Hristov, J. B. Edson, and C. A. Friehe, 2008: Platform motion effects on measurements of turbulence and air–sea exchange over the open ocean. *J. Atmos. Oceanic Technol.*, **25**, 1683–1694, doi:10.1175/2008JTECHO547.1.

——, C. Marandino, and E. S. Saltzman, 2010: Ship-based measurement of air-sea CO_2 exchange by eddy covariance. *J. Geophys. Res.*, **115**, D02304, doi:10.1029/2009JD012193.

Mitsuta, Y., and T. Fujitani, 1974: Direct measurement of turbulent fluxes on a cruising ship. *Bound.-Layer Meteor.*, **6**, 203–217, doi:10.1007/BF00232485.

Nagata, Y., 1964: The statistical properties of orbital wave motions and their application for the measurement of directional wave spectra. *J. Oceanogr. Soc. Japan*, **19**, 169–181, doi:10.5928/kaiyou1942.19.169.

Neumann, T., K. Nolopp, M. Strack, H. Mellinghoff, H. Söker, E. Mittelstaedt, W. J. Gerasch, and G. Fischer, 2003: Erection of German offshore measuring platform in the North Sea. *DEWI Mag.*, **23**, 32–46.

Oncley, S. P., C. A. Friehe, J. C. Larue, J. A. Businger, E. C. Itsweire, and S. S. Chang, 1996: Surface-layer fluxes, profiles, and turbulence measurements over uniform terrain under near-neutral conditions. *J. Atmos. Sci.*, **53**, 1029–1044, doi:10.1175/1520-0469(1996)053<1029:SLFPAT>2.0.CO;2.

Oost, W. A., C. W. Fairall, J. B. Edson, S. D. Smith, R. J. Anderson, J. A. B. Wills, K. B. Katsaros, and J. Decosmo, 1994: Flow distortion calculations and their application in HEXMAX. *J. Atmos. Oceanic Technol.*, **11**, 366–386, doi:10.1175/1520-0426(1994)011<0366:FDCATA>2.0.CO;2.

Prytherch, J., M. J. Yelland, I. M. Brooks, D. J. Tupman, R. W. Pascal, B. I. Moat, and S. J. Norris, 2015: Motion-correlated flow distortion and wave-induced biases in air–sea flux measurements from ships. *Atmos. Chem. Phys.*, **15**, 10 619–10 629, doi:10.5194/acp-15-10619-2015.

Schulz, E. W., B. G. Sanderson, and E. F. Bradley, 2005: Motion correction for shipborne turbulence sensors. *J. Atmos. Oceanic Technol.*, **22**, 55–69, doi:10.1175/JTECH-1685.1.

Smedman, A., U. Högström, H. Bergstrom, A. Rutgersson, K. K. Kahma, and H. Pettersson, 1999: A case study of air-sea interaction during swell conditions. *J. Geophys. Res.*, **104**, 25 833–25 851, doi:10.1029/1999JC900213.

Song, X. L., C. A. Friehe, and D. X. Hu, 1996: Ship-board measurements and estimations of air-sea fluxes in the western tropical Pacific during TOGA COARE. *Bound.-Layer Meteor.*, **81**, 373–397, doi:10.1007/BF02430336.

Stull, R. B., 1988: *An Introduction to Boundary Layer Meteorology*. Kluwer Academic, 666 pp.

Takahashi, S., F. Kondo, O. Tsukamoto, Y. Ito, S. Hirayama, and H. Ishida, 2005: On-board automated eddy flux measurement system over open ocean. *SOLA*, **1**, 37–40, doi:10.2151/sola.2005-011.

Tsukamoto, O., E. Ohtaki, H. Ishida, M. Horiguchi, and Y. Mitsuta, 1990: On-board direct measurements of turbulent fluxes over the open sea. *J. Meteor. Soc. Japan*, **68**, 203–211.

Weller, R. A., S. P. Bigorre, J. Lord, J. D. Ware, and J. B. Edson, 2012: A surface mooring for air–sea interaction research in the Gulf Stream. Part I: Mooring design and instrumentation. *J. Atmos. Oceanic Technol.*, **29**, 1363–1376, doi:10.1175/JTECH-D-12-00060.1.

Wyngaard, J. C., 1981: The effects of probe-induced flow distortion on atmospheric turbulence measurements. *J. Appl. Meteor.*, **20**, 784–794, doi:10.1175/1520-0450(1981)020<0784:TEOPIF>2.0.CO;2.

——, and O. R. Coté, 1972: Cospectral similarity in the atmospheric surface layer. *Quart. J. Roy. Meteor. Soc.*, **98**, 590–603, doi:10.1002/qj.49709841708.

Yelland, M. J., and P. K. Taylor, 1996: Wind stress measurements from the open ocean. *J. Phys. Oceanogr.*, **26**, 541–558, doi:10.1175/1520-0485(1996)026<0541:WSMFTO>2.0.CO;2.

——, B. I. Moat, P. K. Taylor, R. W. Pascal, J. Hutchings, and V. C. Cornell, 1998: Wind stress measurements from the open ocean corrected for airflow distortion by the ship. *J. Phys. Oceanogr.*, **28**, 1511–1526, doi:10.1175/1520-0485(1998)028<1511:WSMFTO>2.0.CO;2.

——, ——, R. W. Pascal, and D. I. Berry, 2002: CFD model estimates of the airflow distortion over research ships and the impact on momentum flux measurements. *J. Atmos. Oceanic Technol.*, **19**, 1477–1499, doi:10.1175/1520-0426(2002)019<1477:CMEOTA>2.0.CO;2.